SUPPLEMENTARY MATERIAL FOR
Cell Atlas of Aqueous Humor Outflow Pathways in Eyes of Humans and Four Model Species Provides Insights into Glaucoma Pathogenesis

Tavé van Zyl, Wenjun Yan, Alexi McAdams, Yi-Rong Peng, Karthik Shekhar, Aviv Regev, Dejan Juric, and Joshua R. Sanes

MATERIALS & METHODS

Tissue Acquisition. Human ocular tissues used for sequencing, immunohistochemistry and *in situ* hybridization were obtained from Massachusetts General Hospital in collaboration with the Rapid Autopsy Program, Susan Eid Tumor Heterogeneity Initiative. Eyes were collected a median of 6 hours postmortem (range 3-14hrs; see **Table S1**). The whole globe was immediately transported to the lab in a humid chamber on ice. Hemisection was performed at the pars plana and the anterior segment was then placed in Ames medium equilibrated with 95% O_2/5% CO_2. For sequencing, the following dissection was performed: after isolation of the anterior segment, the lens, iris, and ciliary body were removed with a gentle peeling method. The corneoscleral button was hemisected and a small wedge was set aside for fixation. Approximately 9 clock hours (or 270 degrees) of TM tissue was peeled from the scleral sulcus of the remaining tissue with jewelers' forceps. A permissive dissection technique allowed for adjacent tissue from the ciliary muscle to be incorporated into the collection tube if it was liberated in conjunction with the TM strip.

Other human corneoscleral buttons used for IHC and *in situ* hybridization were provided by the Lions Vision Gift (Portland, OR) and were collected <16 hr postmortem and fixed in ice-cold 4% PFA. No ocular disease was reported in any of the human donors and no abnormalities were noted during microdissection. Donor details are provided in Table S2.

Non-human primate eyes were obtained from macaques 4 to 10 years of age that had reached the end of unrelated studies at supplying institutions. No ocular or visual abnormalities were noted. Data presented in this manuscript did not covary with any treatment that had been applied to the animals. For sequencing, two eyes from one female crab-eating macaque (*Macaca fascicularis*, 6 years of age) were used, and two eyes from one male rhesus macaque (*Macaca mulatta*). Eyes were collected either pre-mortem under deep anesthesia or post-mortem (≤ 45 min), after which a rapid hemisection was performed and the anterior immediately placed in ice-cold Ames solution (Sigma-Aldrich; equilibrated with 95% O_2/5% CO_2 for all use), where they were stored before experimentation. Experiments described below commenced within 6 hours of death.

Porcine (*Sus scrofa*) eyes were obtained from a local abattoir, transported back to the lab in a humid chamber on ice, and dissected as above. For sequencing, 2 eyes from 2 individual pigs were used. Due to the porcine iridocorneal anatomy, TM strips were not dissected, and instead, corneoscleral wedges were trimmed and digested *in toto*.

Mouse eyes were collected from male and female 12-week-old CD1 mice obtained from Charles River Laboratories. After euthanasia, eyes were enucleated and transferred to Ames medium equilibrated with 95% O_2/5% CO_2. The anterior segment was dissected from the posterior portion of the eye with microscissors, and the lens was gently removed with forceps. The entire anterior segment, including cornea, iris, ciliary body, and the TM was digested.

Single cell isolation. Tissues were digested enzymatically for 30 minutes at 37°C with papain (Worthington, LS003126) 20 units/mL in Ames. Following digestion, the tissues were triturated into single cell suspensions with 0.15% ovomucoid and 0.04% bovine serum albumin (BSA) in Ames solution and filtered through a 40 µm strainer. Single cell suspensions were diluted at a concentration of 500-1800 cells/µL in 0.04% non-acetylated BSA/Ames for loading into 10X Chromium Single Cell Chips (64). Data were obtained using both v2 and v3 kits and specified in **Table S1**.

Droplet-based scRNA-seq. Single cell libraries were generated with either Chromium 3' v2 or v3 chemistry (10X Genomics, Pleasanton, CA) following the manufacturer's protocol. Briefly, single cells were partitioned into Gel bead in Emulsion (GEMs) in the GemCode instrument with cell lysis and barcoded reverse transcription of RNA, followed by amplification, shearing and 5' adaptor and sample index attachment. On average, approximately 10,000 single cells were loaded on each channel and approximately 6,000 cells were recovered. Libraries were sequenced on Illumina HiSeq 2500.

Histology. See **Table S2** for donor information. Corneoscleral wedges were fixed in 4% PFA for 2-24 hr, transferred to PBS, sunk in 30% sucrose overnight, then embedded in tissue freezing medium and mounted onto poly-d-lysine coated slides in 20 µm meridional sections with ProLong Gold Antifade (Invitrogen). For IHC, slides were incubated for 1 hr in protein block, overnight with primary antibodies, and 2 hr with secondary antibodies. Initial block and secondary antibody incubation were done at room temperature and primary antibody incubation at 4°C. Single molecule fluorescent *in situ* hybridization was performed using commercially available RNAScope Multiplex Fluorescent Assay V2 (Advanced Cell Diagnostics, Newark, CA). Briefly, slides were baked at 60°C for 30 minutes and incubated for 10 minutes at RT with hydrogen peroxide. Two Protease III incubations were performed (30 min, then 15 min). Probe hybridization and subsequent steps were per standard manufacturer protocol. Antibodies and *in situ* probes are catalogued in **Table S3.**

Image acquisition, processing and analysis. Images were acquired on Zeiss LSM 710 confocal microscopes with 405, 488-515, 568, and 647 nm lasers, processed using Zeiss ZEN software suites, and analyzed using ImageJ (NIH). Images were acquired

with 20X, 40X or 100X oil lens at the resolution of 1024X1024 pixels, a step size of 1.0 μm, and 90 μm pinhole size.

Computational Methods.
Clustering analysis: Sequencing data was demultiplexed and aligned using the cellranger (10X Genomics) mkfastq and count functions respectively (cellranger version 2 for samples collected with v2 kit and version 3 for samples collected with v3 kit). Reads were aligned to the following reference genome: Human samples-GRCh38, Macaca Mulatta-Mmul8, Macaca Fascicularis-MacFas5 with our augmented transcriptome file (65), Pig-Sscrofa11, Mouse-mm10. The number of genes/transcripts detected per cell was plotted for every sample and a threshold was chosen based on their distributions for each species. Cells with fewer than 600 genes were excluded from further analysis for primates and pig; the threshold for mouse was 1000 genes/cell.

The analysis pipeline follows methods described by Peng *et al*. (65). For each species, the Unique Molecular Identifier (UMI) count matrix was normalized by the total number of UMI counts for each cell and multiplied by a scale factor, representing the median UMI counts of the group to correct library size differences. The normalized UMI count matrix was then log transformed after adding 1. High Variable Genes (HVG) were identified using method described in Pandey *et al*. (66). For every gene, the mean (μ) and coefficient of variation (CV) of UMI counts among cells within each group was calculated. The excess CV (eCV) was measured by subtracting the predicted value from a Poisson-Gamma mixture based null model of CV v.s. μ. HVGs were defined as genes whose eCV>[mean of eCV] + 1.3*[SD of eCV]. Batch correction was performed on the expression matrix of HVGs using linear regression model adapted from the 'RegressOut' function in the 'Seurat' R package.

Principal Component analysis (PCA) was performed on the batch-corrected expression matrix of the HVGs. The top 90 PCs were calculated using the 'irlba' R package on centered and scaled data. Statistically significant PCs were estimated based on the Tracy-Widom distribution (67). The PCA-reduced data was projected to 2D using t-distributed stochastic neighbor embedding (t-SNE) for visualization. Unsupervised Louvain-Jaccard clustering method was applied to cells in the PCA reduced dimensional space of the significant PCs (68). Clusters formed by either low quality cells or doublets were removed before further analysis. Clusters containing low quality cells could be identified by a combination of the following: lower median number of genes/transcripts per cell, higher proportion of reads from mitochondrial genes, and lack of uniquely expressed genes. Clusters containing doublets could be identified by their overall higher number of genes/transcripts than other clusters, high expression levels of marker genes from multiple cell types, and also lack of uniquely expressed genes.

To assess the overall relationships among clusters, a dendrogram was built in each species using normalized expression matrix of HVGs. To correct for potential over-clustering due to batch effect, or the lack of computation power in distinguishing types, the following steps were taken. To address the first issue, cluster pairs that were located closest to each other on the dendrogram were tested, and they were merged iteratively until sufficient differences were found between the current cluster pair (≥5 DE genes

enriched both ways, log fold-change >1.2, adjusted p value < 0.001; statistical testing was performed using the 'MAST' R package). After each merge, a new dendrogram was built for testing the new pair. To address the second issue, sub-clustering was performed on each cluster with newly defined HVGs among cells and using previous described testing method for verification.

In most cases, result from sub-clustering represented over-clustering; however, in some cases, we were able to distinguish real types (i.e. the human Schlemm canal and collector channel cells were grouped as one cluster at the initial clustering, but split into two at the sub-clustering step). In other cases, the lack of clustering power was due to limited sample size, as for all the species we analyzed except the human. Referring to the cross-species mapping (described below) to first spot the cluster as a potential cell type mixture in non-human dataset, we used supervised methods to separate them with type markers found in human. For example, the Schlemm canal and collector channel in *M. fascicularis* were initially clustered as a single type using unsupervised methods, but the human type markers were present in separate cell populations (***Figure S5B***), allowing us to split the cluster. Subsequently, criteria described above were applied to verify the new clusters. Due to differences in the dissection method, we obtained a large amount of corneal epithelium from our mouse collection. The presence of these cells saturated the dynamic range in feature space and weakened our computational power in classification of other types; therefore, the majority of corneal epithelium was removed at the initial analysis.

Cross species comparison: To evaluate the transcriptomic similarity between human and other model species, we applied a gradient boosted decision tree algorithm, XGBoost (56) using the 'xgboost' R package. We used the human dataset for training because it was the largest. Classifiers were trained on 80% of the human dataset using the HVGs shared between human and each of the other species. The remaining 20% were used as a validation dataset to evaluate the accuracy of the classifier; for all four classifiers built, the validation accuracies were >95%. Data from non-human species were used as the testing dataset whereby cells that get more than a 16% vote (calculated from the equation below) for the 'winner' type are assigned with human type identity, while those failing to pass the criteria are assigned as 'unmapped'.
The criteria is calculated as promotion of winning votes ≥: $3 \times \frac{1}{\#\ of\ types}$, where # of types in the human dataset is 19. In some cases, a single cluster in the testing dataset might map to two types in the training dataset, and this serves as a clue of potential cell type mixture as mentioned previously. Further sub-clustering and verification was performed accordingly.

Data availability: The accession number for the raw and unprocessed data files reported in this paper is GEO: GSE146188. Data can be visualized at the Broad Institute's Single Cell Portal at https://singlecell.broadinstitute.org/single_cell/study/SCP780.

Study Approval. All animal procedures performed in this study were conducted in compliance with the Association for Research in Vision and Ophthalmology's Statement for the Use of Animals in Ophthalmic and Vision Research and guidelines for the care and use of animals and human subjects at Harvard University and Partners Healthcare. Acquisition and use of human tissue was approved by the Human Study Subject Committees (DFCI Protocol Number: 13-416 and MEE - NHSR Protocol Number 18-034H). Acquisition and use of non-human tissue was approved by the Institutional Animal Care and Use Committee (IACUC) at Harvard University.

SUPPLEMENTARY FIGURE LEGENDS

Figure S1

A. Workflow for obtaining single cell transcriptomes.
B. Dissection procedure. Left: anterior segment following dissection at the pars plana, posterior view. Middle: blunt dissection of TM strip following removal of lens, iris and ciliary body. Right: Strip of isolated TM.

Figure S2 Histological Characterization of Human Outflow Pathways

A. Beam cells immunostained with *PDPN* (green) and *FABP4* (red). Schlemm canal outlined in dashed line. AF, Autofluorescence.
B. Enlargement of boxed area in A.
C. Ciliary muscle cells co-immunostained for CHRM3 (green) and DES (red).
D. Pericytes immunostained for NDUFA4L2 (green), wrapped around a vessel stained with PECAM1 (red).
E. Neuron within the ciliary muscle immunostained for ELAVL4/HuD (red).
F. Mast cells within the TM immunostained for IL1RL1 (green).
G. B cells within the TM immunostained for CD27 (green).
H. Immunostaining against ADH1B (green) highlights scleral fibroblasts in the vicinity of TM and SC. This image is shown in higher magnification in ***Figure 3H***.
I. Fluorescent RNA *in situ* hybridization against *ANGPTL7* (green) and *CHI3L1* (red) highlights cells in the JCT. Schlemm canal outlined in dashed line. A cropped version of this image is shown in higher magnification in ***Figure 3E***.
J. Fluorescent RNA *in situ* hybridization against *TMEFF2* (red) and *PPPR1B1* (green) highlights beam cells. A cropped version of this image is shown in higher magnification in ***Figure 3D***.
K. Fluorescent RNA *in situ* hybridization against *RARRES1* (green) and *CYP1B1* (red) demonstrates positive signal within beam cells > JCT.
L. Enlargement of area boxed in **K**.
Scale bar = 50μm.

Figure S3 Expression of Disease-Associated Genes

Heat map showing expression of genes implicated in glaucoma by key human cell types. Genes detected in more than 10% cells of at least one type were shown.

Expression strength of each gene is row-normalized. TM, trabecular meshwork; CM, ciliary muscle; cEndo, canal endothelium.

Figure S4 Gene Expression in Disease-Relevant Pathways
Dot plot showing human cell-type specific expression patterns of complement factors (**A**); aquaporins (**B**); matrix metalloproteinases (**C**); Rho genes (**D**); Cytochrome P450 enzymes (**E**); and prostaglandin related genes (**F**).

Figure S5 Analysis of cell types and gene expression in M. Fascicularis
A Violin plot showing examples of genes selectively expressed by each cell type in *M. fascicularis.*
B Supervised clustering of Schlemm Canal and collector channels in *M. fascicularis.*
C-H Histological localization of cluster markers in meridional sections of iridocorneal angles from *M. fascicularis* confirms identities of computationally derived cell types. PDPN (red) stains trabecular beams (**C-F**) but also melanocytes within the ciliary muscle (CM) identified through co-staining with *MLANA* (green, **H**); Schlemm canal is outlined with PECAM1+ (red) immunostaining whereas CM is highlighted with immunostaining against DES (green, **G**); CDH19 (green) highlights Schwann cells in CM (**F**). Fluorescent RNA *in situ* hybridization against *RARRES1* (green) and *CYP1B1* (red) highlights cells in the TM (Beams > JCT).
Bars show 50μm in C-E, G and H, and 25μm in F.

Figure S6. Histological characterization of outflow cell types in Pig
A Immunostaining against PECAM1 (green) highlights both the Aqueous plexus (AqP) and a downstream collector channel/scleral vessel whereas LYVE1(red) stains only the AqP.
B Immunostaining against *ACTA2* (green) highlights ciliary muscle and pericytes (asterisk).
C. Immunostaining against *NDUFA4L2* (green) is strongest at the border of iris vessels, indicating pericytes, but also shows weak staining in the TM and corneal endothelium, consistent with transcriptional data.
Bars show 50μm.

Figure S7 Expression of key marker genes in mouse
Violin plots showing expression of key marker genes in mouse.

Figure S8. Comparison of gene expression across species
Key genes are shown in dot plots for cell types comprising the vessel endothelium (**A**) Schwalbe line / Corneal endothelium (**B**) and immune cells (**C**).

SUPPLEMENTARY TABLES

Table S1

Information about human donor eye tissue used for scRNA-seq. Pt, Patient; RT, right eye; LT, left eye; MGH, Massachusetts General Hospital; DTP, death to processing time. Column labeled “10X” refers to the version of the 3’ single cell chemistry (as a commercially available kit from 10X Genomics) utilized for scRNA-seq library preparation.

Table S2

Information about human donor eye tissue used for histological validation. Pt, Patient; RT, right eye; LT, left eye; HCS, human corneoscleral rim; MGH, Massachusetts General Hospital; LVG, Lions Vision Gift; DTP, death to preservation; IHC, immunohistochemistry. Column labeled “RNA *in situ”* indicates RNAScope probes used. Column labeled “IHC” indicates antibody targets used for localization.

Table S3

Antibodies and probes used for histological studies.

REFERENCES CITED IN SUPPLEMENTARY MATERIAL

64. G.X. Zheng *et al.*, Massively parallel digital transcriptional profiling of single cells. *Nat Commun.* **8**, 14049 (2017).

65. Y.R. Peng *et al*., Molecular classification and comparative taxonomics of foveal and peripheral cells in primate retina. *Cell* **176**,1222-1237 (2019).

66. S. Pandey, K. Shekhar, A. Regev, A.F. Schier, Comprehensive identification and spatial mapping of habenular neuronal types using single-cell RNA-seq. *Curr. Biol.* **28**, 1052-1065 (2018).

67. N. Patterson, A.L. Price, D. Reich, Population structure and eigenanalysis. *PLoS Genet.* **2**, e190 (2006).

68. K. Shekhar *et al*. Comprehensive classification of retinal bipolar neurons by single-cell transcriptomics. *Cell* **166**, 1308-1323 (2016).

Figure S1

A

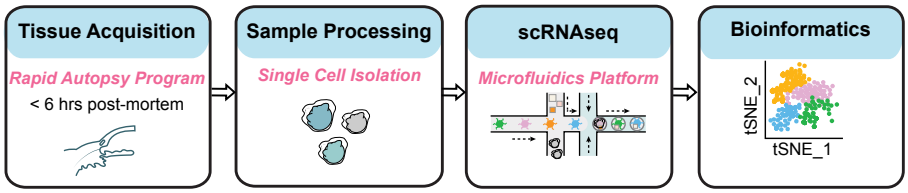
Tissue Acquisition
Rapid Autopsy Program
< 6 hrs post-mortem
Sample Processing
Single Cell Isolation
scRNAseq
Microfluidics Platform
Bioinformatics
tSNE_2
tSNE_1

B

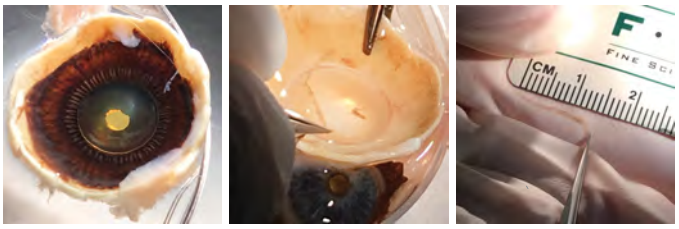

Figure S2

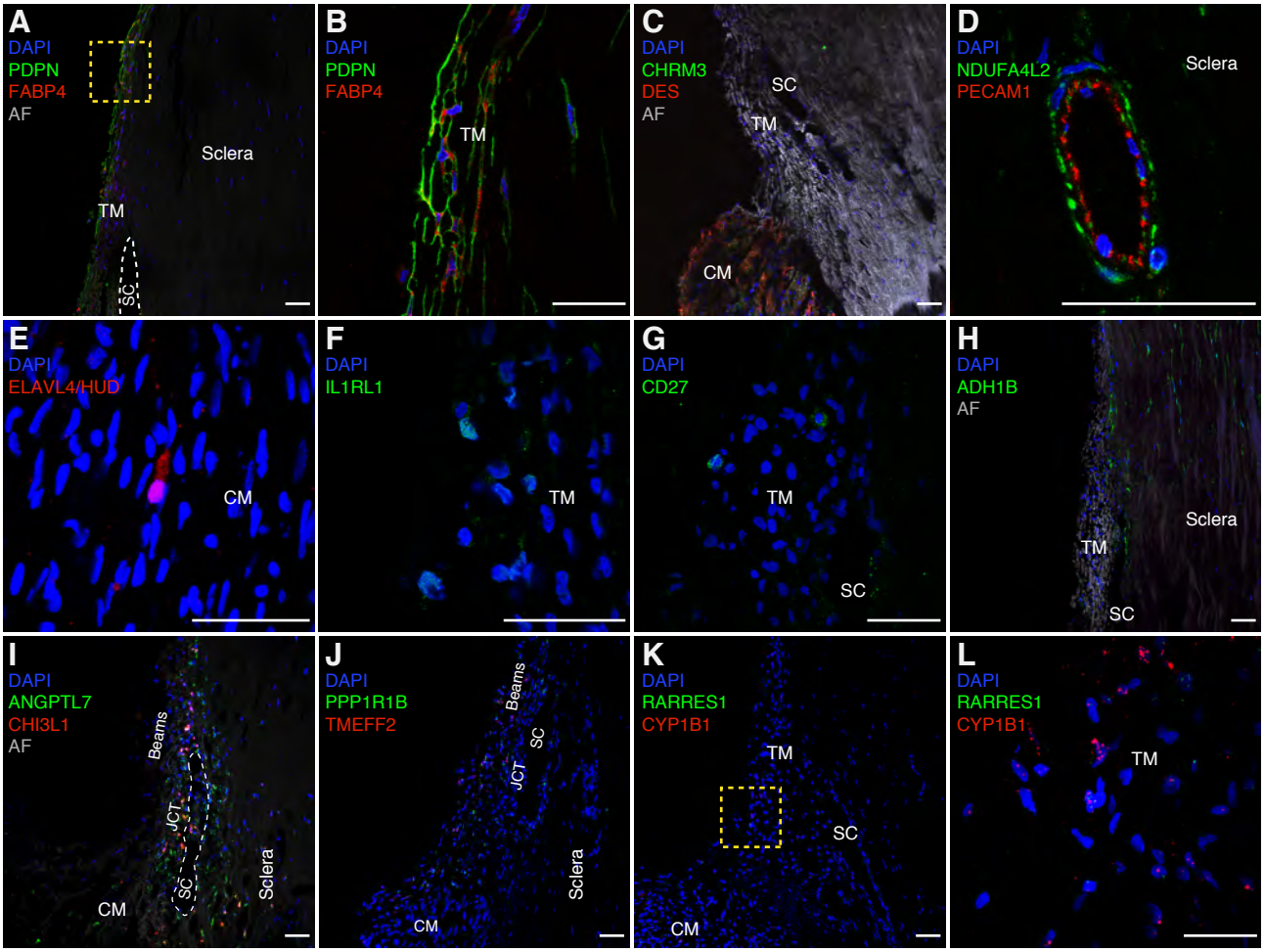
A
DAPI
PDPN
FABP4
AF
Sclera
TM
SC
B
DAPI
PDPN
FABP4
TM
C
DAPI
CHRM3
DES
AF
SC
TM
CM
D
DAPI
NDUFA4L2
PECAM1
Sclera
E
DAPI
ELAVL4/HUD
CM
F
DAPI
IL1RL1
TM
G
DAPI
CD27
TM
SC
H
DAPI
ADH1B
AF
Sclera
TM
SC
I
DAPI
ANGPTL7
CHI3L1
AF
Beams
JCT
SC
Sclera
CM
J
DAPI
PPP1R1B
TMEFF2
Beams
SC
JCT
Sclera
CM
K
DAPI
RARRES1
CYP1B1
TM
SC
CM
L
DAPI
RARRES1
CYP1B1
TM

Figure S3

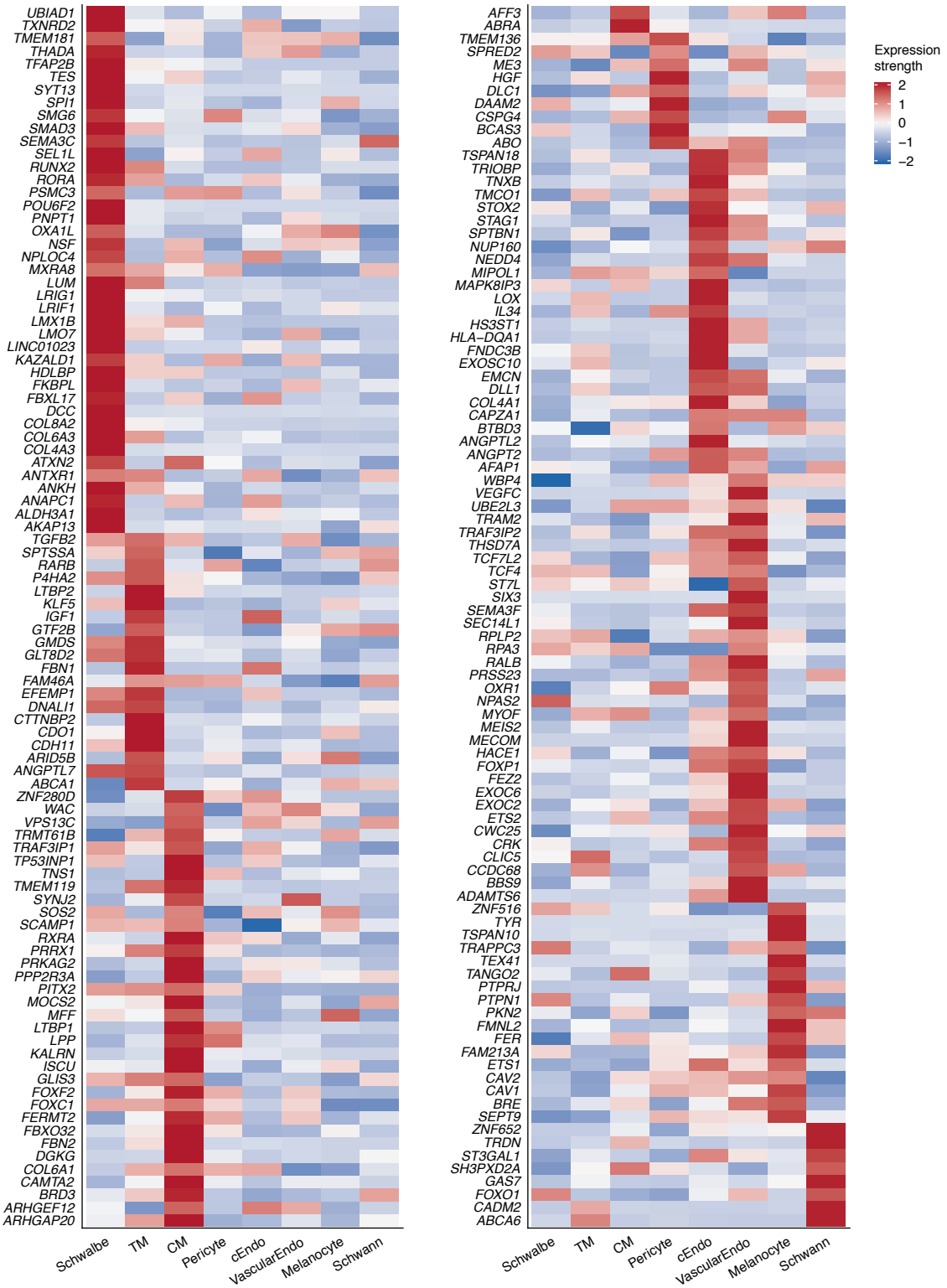
UBIAD1
TXNRD2
TMEM181
THADA
TFAP2B
TES
SYT13
SPI1
SMG6
SMAD3
SEMA3C
SEL1L
RUNX2
RORA
PSMC3
POU6F2
PNPT1
OXA1L
NSF
NPLOC4
MXRA8
LUM
LRIG1
LRIF1
LMX1B
LMO7
LINC01023
KAZALD1
HDLBP
FKBPL
FBXL17
DCC
COL8A2
COL6A3
COL4A3
ATXN2
ANTXR1
ANKH
ANAPC1
ALDH3A1
AKAP13
TGFB2
SPTSSA
RARB
P4HA2
LTBP2
KLF5
IGF1
GTF2B
GMDS
GLT8D2
FBN1
FAM46A
EFEMP1
DNALI1
CTTNBP2
CDO1
CDH11
ARID5B
ANGPTL7
ABCA1
ZNF280D
WAC
VPS13C
TRMT61B
TRAF3IP1
TP53INP1
TNS1
TMEM119
SYNJ2
SOS2
SCAMP1
RXRA
PRRX1
PRKAG2
PPP2R3A
PITX2
MOCS2
MFF
LTBP1
LPP
KALRN
ISCU
GLIS3
FOXF2
FOXC1
FERMT2
FBXO32
FBN2
DGKG
COL6A1
CAMTA2
BRD3
ARHGEF12
ARHGAP20
Schwalbe
TM
CM
Pericyte
cEndo
VascularEndo
Melanocyte
Schwann
AFF3
ABRA
TMEM136
SPRED2
ME3
HGF
DLC1
DAAM2
CSPG4
BCAS3
ABO
TSPAN18
TRIOBP
TNXB
TMCO1
STOX2
STAG1
SPTBN1
NUP160
NEDD4
MIPOL1
MAPK8IP3
LOX
IL34
HS3ST1
HLA-DQA1
FNDC3B
EXOSC10
EMCN
DLL1
COL4A1
CAPZA1
BTBD3
ANGPTL2
ANGPT2
AFAP1
WBP4
VEGFC
UBE2L3
TRAM2
TRAF3IP2
THSD7A
TCF7L2
TCF4
ST7L
SIX3
SEMA3F
SEC14L1
RPLP2
RPA3
RALB
PRSS23
OXR1
NPAS2
MYOF
MEIS2
MECOM
HACE1
FOXP1
FEZ2
EXOC6
EXOC2
ETS2
CWC25
CRK
CLIC5
CCDC68
BBS9
ADAMTS6
ZNF516
TYR
TSPAN10
TRAPPC3
TEX41
TANGO2
PTPRJ
PTPN1
PKN2
FMNL2
FER
FAM213A
ETS1
CAV2
CAV1
BRE
SEPT9
ZNF652
TRDN
ST3GAL1
SH3PXD2A
GAS7
FOXO1
CADM2
ABCA6
Schwalbe
TM
CM
Pericyte
cEndo
VascularEndo
Melanocyte
Schwann
Expression strength
2
1
0
−1
−2

Figure S4

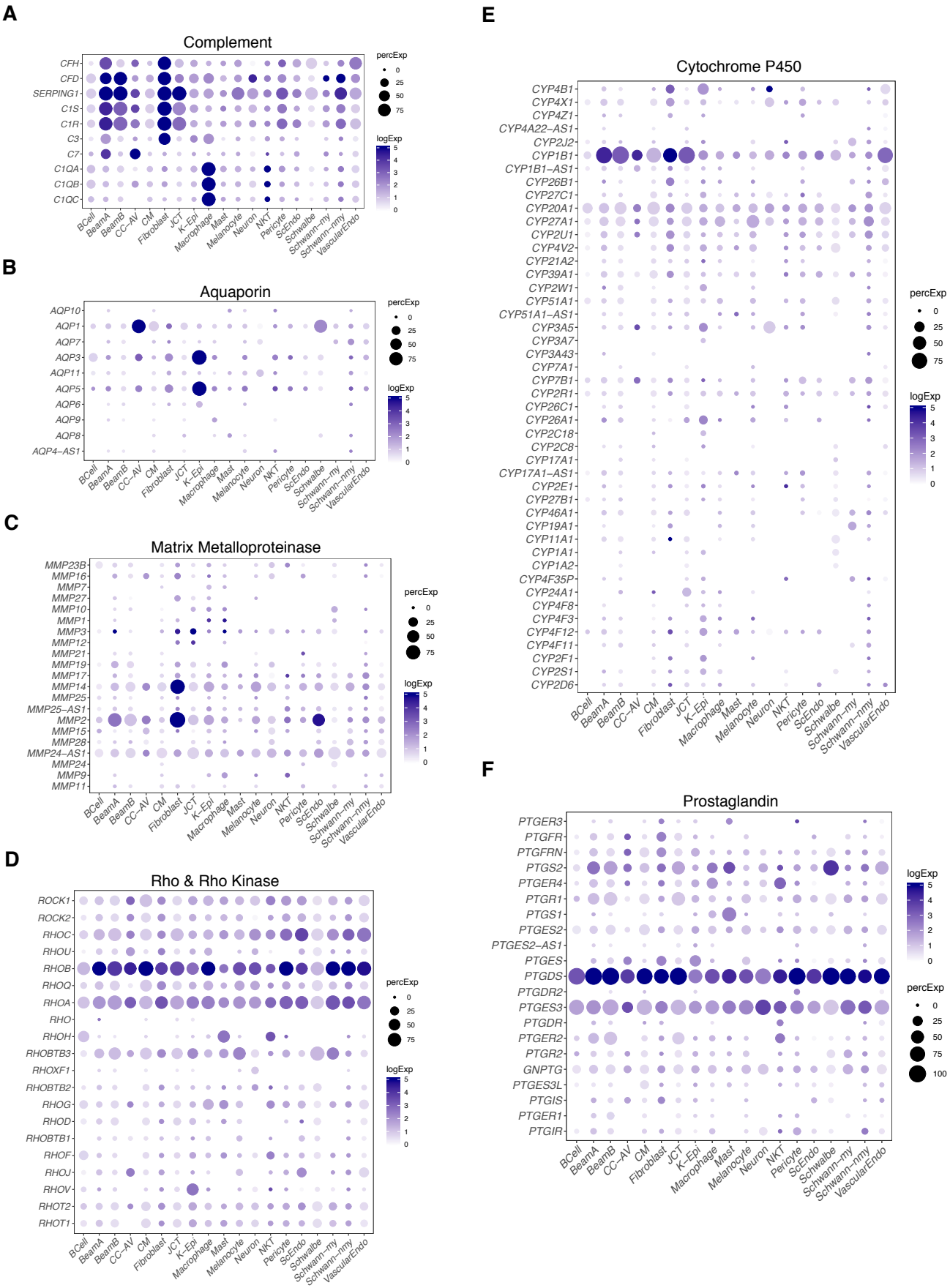
A
Complement
CFH
CFD
SERPING1
C1S
C1R
C3
C7
C1QA
C1QB
C1QC
B
Aquaporin
AQP10
AQP1
AQP7
AQP3
AQP11
AQP5
AQP6
AQP9
AQP8
AQP4–AS1
C
Matrix Metalloproteinase
MMP23B
MMP16
MMP7
MMP27
MMP10
MMP1
MMP3
MMP12
MMP21
MMP19
MMP17
MMP14
MMP25
MMP25–AS1
MMP2
MMP15
MMP28
MMP24–AS1
MMP24
MMP9
MMP11
D
Rho & Rho Kinase
ROCK1
ROCK2
RHOC
RHOU
RHOB
RHOQ
RHOA
RHO
RHOH
RHOBTB3
RHOXF1
RHOBTB2
RHOG
RHOD
RHOBTB1
RHOF
RHOJ
RHOV
RHOT2
RHOT1
E
Cytochrome P450
CYP4B1
CYP4X1
CYP4Z1
CYP4A22–AS1
CYP2J2
CYP1B1
CYP1B1–AS1
CYP26B1
CYP27C1
CYP20A1
CYP27A1
CYP2U1
CYP4V2
CYP21A2
CYP39A1
CYP2W1
CYP51A1
CYP51A1–AS1
CYP3A5
CYP3A7
CYP3A43
CYP7A1
CYP7B1
CYP2R1
CYP26C1
CYP26A1
CYP2C18
CYP2C8
CYP17A1
CYP17A1–AS1
CYP2E1
CYP27B1
CYP46A1
CYP19A1
CYP11A1
CYP1A1
CYP1A2
CYP4F35P
CYP24A1
CYP4F8
CYP4F3
CYP4F12
CYP4F11
CYP2F1
CYP2S1
CYP2D6
F
Prostaglandin
PTGER3
PTGFR
PTGFRN
PTGS2
PTGER4
PTGR1
PTGS1
PTGES2
PTGES2–AS1
PTGES
PTGDS
PTGDR2
PTGES3
PTGDR
PTGER2
PTGR2
GNPTG
PTGES3L
PTGIS
PTGER1
PTGIR
BCell
BeamA
BeamB
CC–AV
CM
Fibroblast
JCT
K–Epi
Macrophage
Mast
Melanocyte
Neuron
NKT
Pericyte
ScEndo
Schwalbe
Schwann–my
Schwann–nmy
VascularEndo
percExp
logExp

Figure S5

A

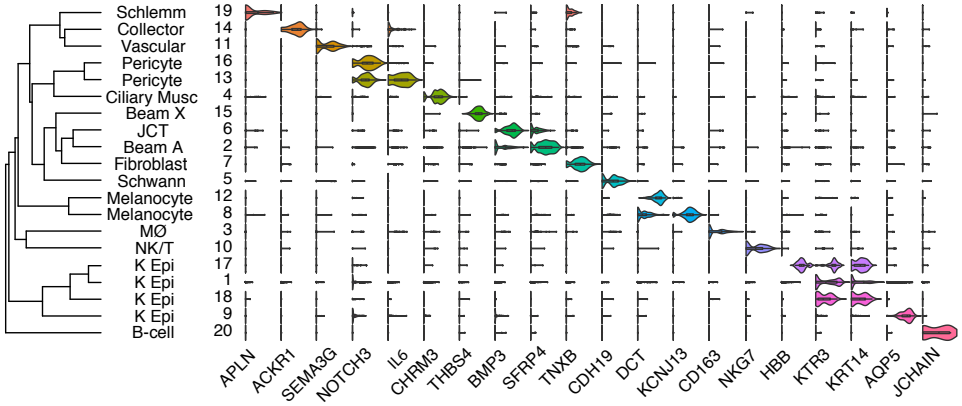
Schlemm 19
Collector 14
Vascular 11
Pericyte 16
Pericyte 13
Ciliary Musc 4
Beam X 15
JCT 6
Beam A 2
Fibroblast 7
Schwann 5
Melanocyte 12
Melanocyte 8
MØ 3
NK/T 10
K Epi 17
K Epi 1
K Epi 18
K Epi 9
B-cell 20
APLN
ACKR1
SEMA3G
NOTCH3
IL6
CHRM3
THBS4
BMP3
SFRP4
TNXB
CDH19
DCT
KCNJ13
CD163
NKG7
HBB
KTR3
KRT14
AQP5
JCHAIN

B

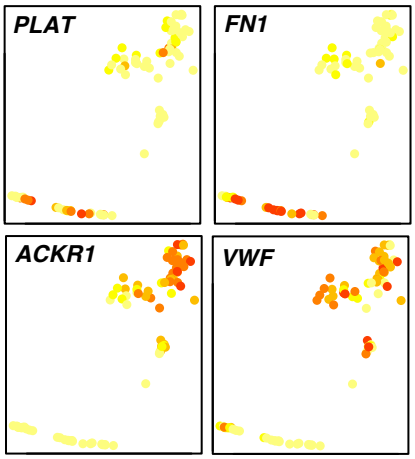
PLAT
FN1
ACKR1
VWF

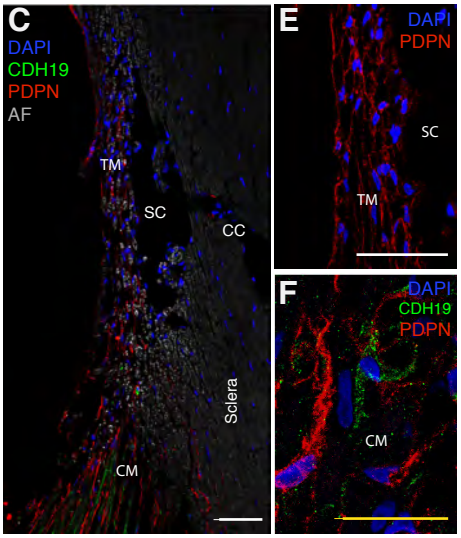
C
DAPI
CDH19
PDPN
AF
TM
SC
CC
Sclera
CM
E
DAPI
PDPN
SC
TM
F
DAPI
CDH19
PDPN
CM
D
DAPI
DES
PECAM1
AF
TM
SC
CM
G
DAPI
RARRES1
CYP1B1
Beams
JCT
H
DAPI
MLANA
PDPN
CM

Figure S6

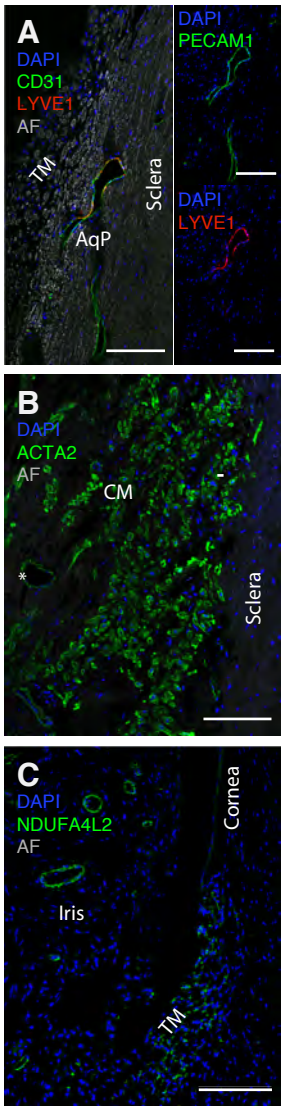
A
DAPI
CD31
LYVE1
AF
TM
AqP
Sclera
DAPI
PECAM1
DAPI
LYVE1
B
DAPI
ACTA2
AF
CM
*
Sclera
C
DAPI
NDUFA4L2
AF
Iris
TM
Cornea

Figure S7

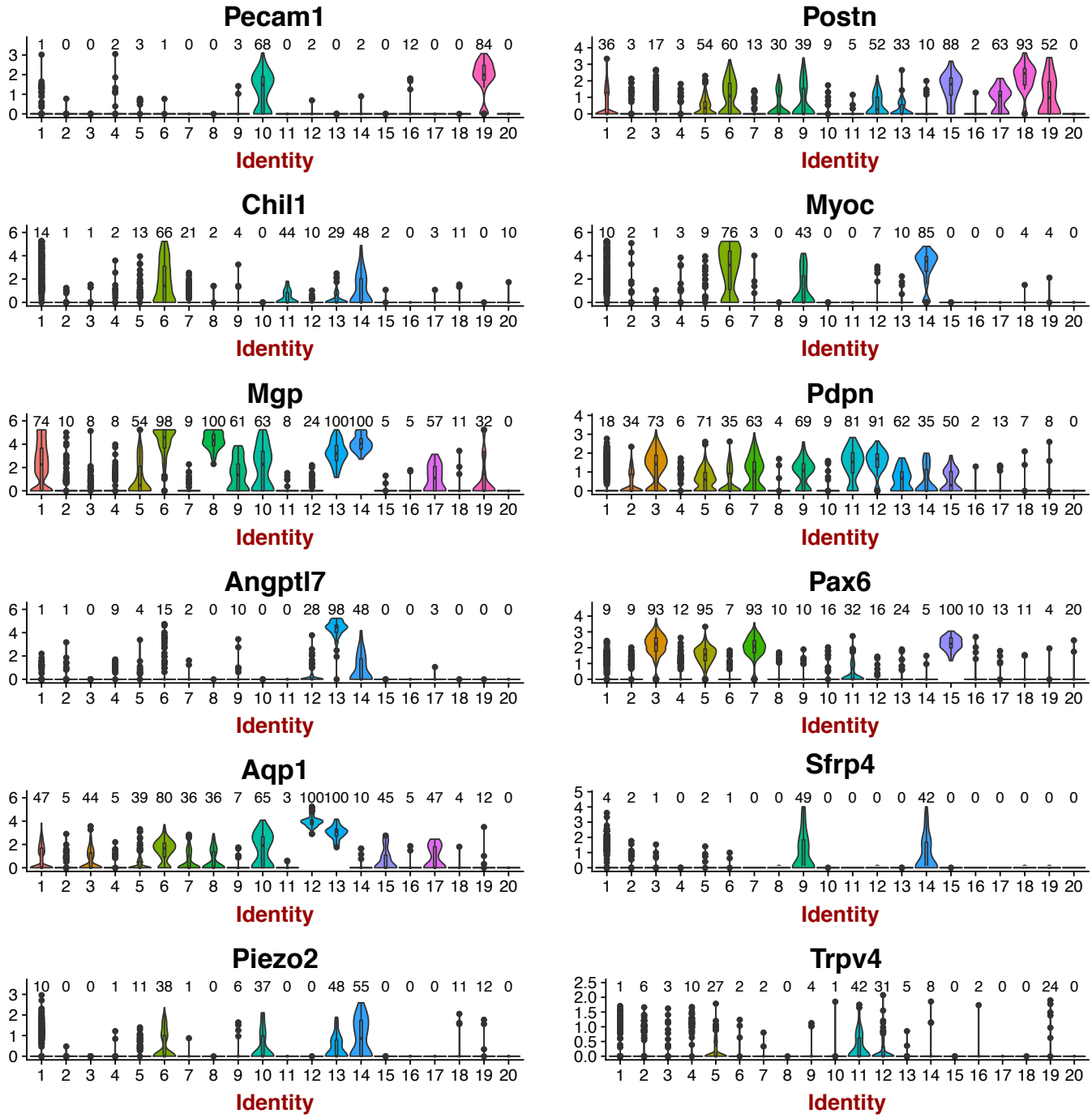
Pecam1
Postn
Chil1
Myoc
Mgp
Pdpn
Angptl7
Pax6
Aqp1
Sfrp4
Piezo2
Trpv4
Identity

Figure S8

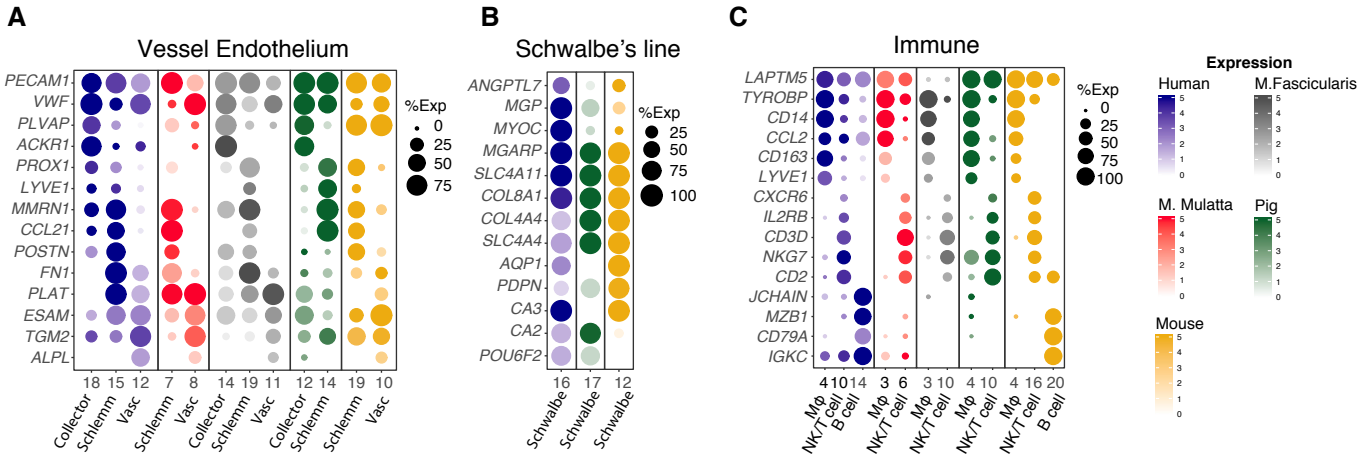
A
Vessel Endothelium
PECAM1
VWF
PLVAP
ACKR1
PROX1
LYVE1
MMRN1
CCL21
POSTN
FN1
PLAT
ESAM
TGM2
ALPL
%Exp
0
25
50
75
18 15 12 7 8 14 19 11 12 14 19 10
Collector Schlemm Vasc Schlemm Vasc Collector Schlemm Vasc Collector Schlemm Schlemm Vasc
B
Schwalbe's line
ANGPTL7
MGP
MYOC
MGARP
SLC4A11
COL8A1
COL4A4
SLC4A4
AQP1
PDPN
CA3
CA2
POU6F2
%Exp
25
50
75
100
16 17 12
Schwalbe Schwalbe Schwalbe
C
Immune
LAPTM5
TYROBP
CD14
CCL2
CD163
LYVE1
CXCR6
IL2RB
CD3D
NKG7
CD2
JCHAIN
MZB1
CD79A
IGKC
%Exp
0
25
50
75
100
4 10 14 3 6 3 10 4 10 4 16 20
Mφ NK/T cell B cell Mφ NK/T cell Mφ NK/T cell Mφ NK/T cell Mφ NK/T cell B cell
Expression
Human
M.Fascicularis
M. Mulatta
Pig
Mouse

Table S1. Donor Information (scRNA-seq)

Label	Source	10X	Age	Sex	Cause of Death	DTP (Hours)	Sample ID
Pt1-LT	MGH	v2	74	M	Lung cancer	6	H1TM1
Pt2-RT	MGH	v2	78	M	Metastatic melanoma to brain	14	H2TM1
Pt2-LT	MGH	v2	78	M	Metastatic melanoma to brain	14	H2TM2
Pt3-RT	MGH	v2	60	M	Left tonsillar squamous cell carcinoma metastatic to brain and left orbit	6.5	H3TM1
Pt4-LT	MGH	v2	64	M	Diffuse B cell lymphoma spread to thorax and epigastrum	5	H4TM1
Pt9-LT	MGH	v2	53	F	Interstitial Lung Disease	5	H9RimS1
Pt11-RT	MGH	v3	65	M	Metastatic melanoma	3	H11TM1

Table S2. Donor Information (Histology)

Label	Source	Age	Sex	Cause Of Death	DTP (hours)	RNA *in situ*	IHC
Pt5-LT	MGH	44	F	Diffuse B cell lymphoma	5	N/A	LYVE1, CD163, CHRM3, DES
Pt6-LT	MGH	69	M	Metastatic melanoma	3	PPP1R1B, TMEFF2, TFF3, POSTN	CALB2, IL1RL1, CD27
Pt7-LT	MGH	52	F	Traumatic brain hemorrhage	4	ANGPTL7, CHI3L1	N/A
Pt10-RT	MGH	76	M	Metastatic melanoma	7	N/A	PDPN and PECAM1
Pt11-RT	MGH	65	M	Metastatic melanoma	3	RARRES1, CYP1B1	N/A
HCS6-RT	LVG	26	F	Acute respiratory failure	10	N/A	CDH19, DES
HCS13-LT	LVG	22	F	Multiorgan failure	10	N/A	ACKR1, PECAM1, DES, MLANA, HUD
HCS15-RT	LVG	87	F	Hemorrhagic shock	9	N/A	PECAM1, ALPL
HCS17-RT	LVG	42	M	Upper gastrointestinal bleed, cirrhosis	23.5	N/A	PDPN, AQP1
HCS18-LT	LVG	62	F	Sepsis	18	N/A	NDUFA4L2, PECAM1
HCS19-RT	LVG	62	F	Sepsis	18	N/A	RARRES1, PDPN, FABP4, ADH1B

Table S3. Antibodies and probes used for histological studies

Antibody/Probe	**Source**	**Identifier**
Goat Polyclonal anti-Desmin	R&D Systems	Cat #AF3844
Rabbit Polyclonal anti-CD31/Pecam-1	Novus Biologicals	Cat #NB100-2284
Mouse Monoclonal anti-alcohol dehydrogenase 1B	Novus Biologicals	Cat #NBP2-00649
Sheep Polyclonal anti-Podoplanin	R&D Systems	Cat #AF3670
Rabbit Monoclonal anti-FABP4	Abcam	Cat #ab92501
Rabbit Polyclonal anti-RARRES1	LifeSpan BioSciences	Cat #LS-C402827
Goat Polyclonal anti-DARC	Novus Biologicals	Cat #NB100-2421
Rabbit Polyclonal anti-Periostin	ThermoFisher Scientific	Cat #PA5-34641
Rabbit Polyclonal anti-AQP1	Proteintech	Cat #20333-1-AP
Mouse Monoclonal anti-Melan-A	Proteintech	Cat #60348-1-lg
Goat Polyclonal anti-LYVE-1	R&D Systems	Cat #AF2089
Mouse Monoclonal anti-CD163	R&D Systems	Cat #MAB1607
Rabbit Polyclonal anti-Calretinin	Swant	Cat #7697
Rabbit Polyclonal Anti-NDUFA4L2	LifeSpan BioSciences	Cat #LS-B9847
Rabbit Polyclonal Anti-HuD	ThermoFisher Scientific	Cat #PA5-79199
Rabbit Polyclonal Anti-Cadherin 19	LifeSpan BioSciences	Cat #LS-C354596
Goat Polyclonal Anti-Alkaline Phosphatase	ThermoFisher Scientific	Cat #PA5-47419
Rabbit Polyclonal Anti-Podoplanin	LifeSpan BioSciences	Cat #LS-B15911
Hamster Monoclonal Anti-Podoplanin-647	Novus Biologicals	Cat #NB600-1015AF647
RNAscope® Probe-Hs-TMEFF2	ACDBio	Cat #519741
RNAscope® Probe-Hs-PPP1R1B	ACDBio	Cat #477021
RNAscope® Probe-Hs-CHI3L1	ACDBio	Cat #408121
RNAscope® Probe-Hs-ANGPTL7	ACDBio	Cat #552811
RNAscope® Probe-Hs-CYP1B1	ACDBio	Cat #457621
RNAscope® Probe-Hs-RARRES1	ACDBio	Cat #494851